



Cite this: *RSC Adv.*, 2023, 13, 24519

# Crosslinking of a polycaprolactone/tourmaline scaffold by sodium stearate with improved mechanical strength and bioactivity

Dongying Li, Haocheng Du, Wenmin Guo, Meigui Chen,\* Xiaoping Guo, Pin Li, Yanrong Zhou, Peng Chen, Mengqi Li\* and Yong Xu \*

Although polycaprolactone (PCL) matrix composites have been extensively studied, the weak interface with nanofillers limits their further applications in bone tissue engineering. Herein, this study has designed a porous bone scaffold model using the triply periodic minimal surfaces (TPMS), and the optimal porosity was determined by comparing the mechanical properties. A sodium stearate-modified PCL/tourmaline (PCL/TM) composite scaffold with a strong interfacial effect was prepared by selective laser sintering technology. Wherein, sodium stearate acts as a bridge to improve the interaction between TM and PCL interface, while promoting its uniform dispersion. The results showed that the PCL/3% modified TM specimens exhibit the optimum mechanical properties, and their ultimate tensile and compressive strength increases by 21.8% and 32.1%, respectively, compared with pure PCL. The factors of mechanical enhancement of composite scaffolds can be elaborated from the construction of interface bridges. On the one hand, the carboxyl group at one end of sodium stearate will interact with the hydroxyl group on the surface of TM to enhance interfacial adsorption by forming ionic bonds and hydrogen bonds. On the other hand, the hydrophobic long chain at the other end of sodium stearate is universally compatible with hydrophobic PCL, thereby improving the dispersion of TM. These characteristics make the PCL/TM composite scaffold a valuable reference for its application in bone tissue engineering.

Received 26th June 2023  
Accepted 7th August 2023

DOI: 10.1039/d3ra04273a

rsc.li/rsc-advances

## 1 Introduction

The demand for bone implants is increasing due to the frequent occurrence of bone defects, while autologous or allogeneic bone grafting is constrained by limited sources or immune rejection, respectively.<sup>1</sup> In contrast, artificial bone is attracting attention because it has a wide range of material sources and can obtain biological, mechanical, and degradation properties comparable to natural bone by modulating components.<sup>2,3</sup> Polycaprolactone (PCL) has been of great interest in bone tissue engineering due to its good biocompatibility, degradability, and processability.<sup>4–6</sup> However, some studies have shown that pure PCL scaffolds present challenges in terms of mechanical properties and biomineralization as bone implants.<sup>7,8</sup> To overcome these issues, researchers have conducted relevant experimental studies. Wachirahuttapong *et al.*<sup>9</sup> expected to obtain a reinforced composite by introducing polylactic acid (PLA) into PCL, but the effect did not appear to be ideal. The study by Wu *et al.*<sup>10</sup> found that calcium silicate can significantly improve the degradation and bone regeneration ability of PCL scaffolds. The above studies showed that the addition of an effective

enhancement phase is a feasible way to improve PCL performance.

Silicate materials are considered a potential candidate for an effectively enhanced phase due to their inherent high stiffness, good biodegradability, and osteogenesis inducibility.<sup>11</sup> Tourmaline (TM) is a polar crystalline material, belonging to a silicate mineral complexed with multiple elements, with the following chemical formula:  $XY_3Z_6Si_6O_{18}(BO_3)_3W_4$  (where X is  $Na^+$ ,  $Ca^{2+}$ ,  $K^+$  or vacancy; Y is  $Mg^{2+}$ ,  $Fe^{2+}$ ,  $Mn^{2+}$ ,  $Al^{3+}$ ,  $Fe^{3+}$ ,  $Mn^{3+}$ ,  $Li^+$ ; Z is  $Al^{3+}$ ,  $Fe^{3+}$ ,  $Cr^{3+}$ ,  $Mg^{2+}$ ; W is  $OH^-$ ,  $F^-$ ,  $O^{2-}$ ).<sup>12,13</sup> TM has the property of releasing negative ions, which are an air vitamin that protects the heart and brain from blood vessels and has health care benefits.<sup>14</sup> Bin Yu *et al.*<sup>15</sup> filled TM into PLA and found that the melt-blown (MB) nonwoven-containing TM particles had good crystallinity and mechanical properties. Unfortunately, TM as an enhanced phase still faces problems such as intra-matrix aggregation and weak interface effects caused by high surface energy and needs to be solved urgently.<sup>16</sup>

In recent years, the incorporation of chemical functionalities into the reinforcing phase to tackle challenges like uneven dispersion and weak interfacial bonding has gained widespread acceptance. For instance, P. Georgopoulos *et al.*<sup>17</sup> introduced a polydopamine (PDA) coating on the surface of  $TiO_2$ /poly(vinyl butyral) composite material. The results indicated the

Key Laboratory of Hunan Province for Efficient Power System and Intelligent Manufacturing, College of Mechanical and Energy Engineering, Shaoyang University, Shaoyang 422000, China. E-mail: xuyong2927@hnsyu.edu.cn; sciencefield@163.com



formation of hydrogen bonding between PDA and poly(vinyl butyral). Compared to the composite material without the chemical functionality of PDA, the hardness and Young's modulus increased by 38% and 27%, respectively. Xue Yang *et al.*<sup>18</sup> used span-60 to react with TM powder in toluene at 60 °C for 1 h. Long-chain alkyl groups were introduced on the surface of TM by this reaction and SEM images showed that the modified TM became better dispersed in PP. Yingmo Hu *et al.*<sup>19</sup> used stearic acid and toluenesulfonic acid to react with TM at 80 °C for 6 h. Long-chain alkyl groups were introduced on the surface of TM by this reaction which reduced the TM's surface polarity. This reaction introduced stearyl groups on TM's surface and increased TM negative ion release, while agglomeration was significantly reduced. Since toluene is volatile and low toxic, it may pose a risk to human health. Sodium stearate, as the main component of soap, is easily extracted and nontoxic.<sup>20,21</sup> More importantly, it can be modified by a short gentle reaction in a 40 °C water bath,<sup>21</sup> which is expected to be an effective modifier to improve the relationship between the enhanced phase and the matrix.

In addition to materials, the structural design of scaffolds is also an important area of research. In recent years, research focusing on utilizing cellular structures to address engineering challenges in nature has captured the interest of scientists. For example, solution etching can yield nano-channels with spiral structures,<sup>22</sup> and there are also lattice structure designs based on triply periodic minimal surfaces (TPMS).<sup>23</sup> TPMS allows for the mathematical derivation of lattice designs, enabling control over pore size, porosity, and the formation of high-strength structures in porous scaffolds. With the rapid development of additive manufacturing (AM) has greatly facilitated the production of geometrically complex and adjustable-sized biocompatible scaffolds.<sup>24</sup> AM methods have found various applications in biomedical engineering due to their ability to effectively control the topological structure of tissue-engineered porous scaffolds.<sup>25–27</sup> This advancement holds potential applications in bone tissue engineering and implant scaffolding.<sup>28</sup> Therefore, the combination of TPMS and AM is expected to realize the integration of bionic artificial bone from structural design to manufacturing.

This study presents a theoretical model for designing complex porous bone scaffolds using triply periodic minimal surfaces (TPMS). Selective laser sintering (SLS) was employed to manufacture pure PCL scaffolds, and a systematic comparison of structures with different porosities was conducted to assess their impact on the mechanical performance of the scaffolds. The optimum porosity was determined and used as the structure for the subsequent manufacture of the PCL/TM composite scaffold. Another work was to modify TM powder with sodium stearate and test the properties of the powder before and after modification. Importantly, the mechanism behind the sodium stearate-modified TM-enhanced composite scaffold mechanical properties was explored. Furthermore, the biodegradability and *in vitro* mineralization capacity of the scaffolds were evaluated by soaking them in phosphate-buffered saline (PBS) and simulated body fluid (SBF).

## 2 Materials and methods

### 2.1 Design of Gyroid TPMS

There are various approaches for constructing TPMS, including image-based methods, space-fitting methods, surface generation based on implicit functions, and CAD-based methods. In this study, a Gyroid(G) TPMS with a cubic unit cell was designed using MS Lattice software, which relies on implicit functions that can be approximated using the following trigonometric functions:

$$F_{G(x,y,z)} = \sin(\omega_x x) \cos(\omega_y y) + \sin(\omega_y y) \cos(\omega_z z) + \sin(\omega_z z) \cos(\omega_x x) = C \quad (1)$$

where  $\omega_x$ ,  $\omega_y$ ,  $\omega_z$  represents the periodicity of the G expression and can also be expressed as:

$$\omega_i = \frac{2\pi}{n_i/l_i} \quad (\text{where, } i = x, y, z) \quad (2)$$

where  $n_i$  represents the number of unit repetitions in the  $x$ ,  $y$ , and  $z$  coordinates,  $l_i$  represents the absolute dimensions in these directions, and  $C$  represents the ISO value (level set constant), which determines a specific surface and can control the volume fraction of pores. For most TPMS structures, there is a linear relationship between  $C$  and relative density (RD).

Therefore, assigning a random value to  $C$  can generate a structure with a specific relative density (RD):

$$G \text{ sheet networks: } C = (RD + 1.806)/67.91 \quad (3)$$

By solving eqn (3) and adjusting the value of  $C$ , different relative densities can be obtained. Using these values, G TPMS structures with a lattice size of  $1 \times 1 \times 1$  mm and relative densities ranging from 10% to 50% can be generated. Then, all the files can be saved and exported using MS Lattice. As shown in Fig. 1a, by varying the value of  $C$ , lattice structures with relative densities ranging from 10% to 50% were obtained.

To evaluate the mechanical performance, such as compressive strength. Cylindrical models corresponding to RD values were constructed separately, as shown in Fig. 1b. To save computational costs (time and memory), the cylindrical model with dimensions of  $\varnothing 4 \times 4$  mm<sup>3</sup> was generated. Observing the surface of the cylinder, it was noticed that the thickness ( $t$ ) of the lattice gradually increased with the increase in RD value. Conversely, the porosity ( $p$ ) of the lattice decreases from 90% to 50%. When designing scaffolds with a porous structure, the surface-to-volume ratio (S/V) is an important parameter. Studies have shown that a larger surface area can improve cell adhesion, bone growth, and promote cell proliferation indicators. Table 1 presents the relationship between the strut thickness ( $t$ ) of the G structure and the scaffold's relative density (RD) and S/V ratio.

In Fig. 1c, scaffold designs of different structural types were created based on G TPMS unit cells. The human femur was reconstructed through CT scanning and exported as an STL file, which could be contained within a cube measuring  $56 \times 82 \times 95$  mm<sup>3</sup>. The G lattice can be used to fill or merge arbitrary 3D models, resulting in complex 3D models based on G TPMS as



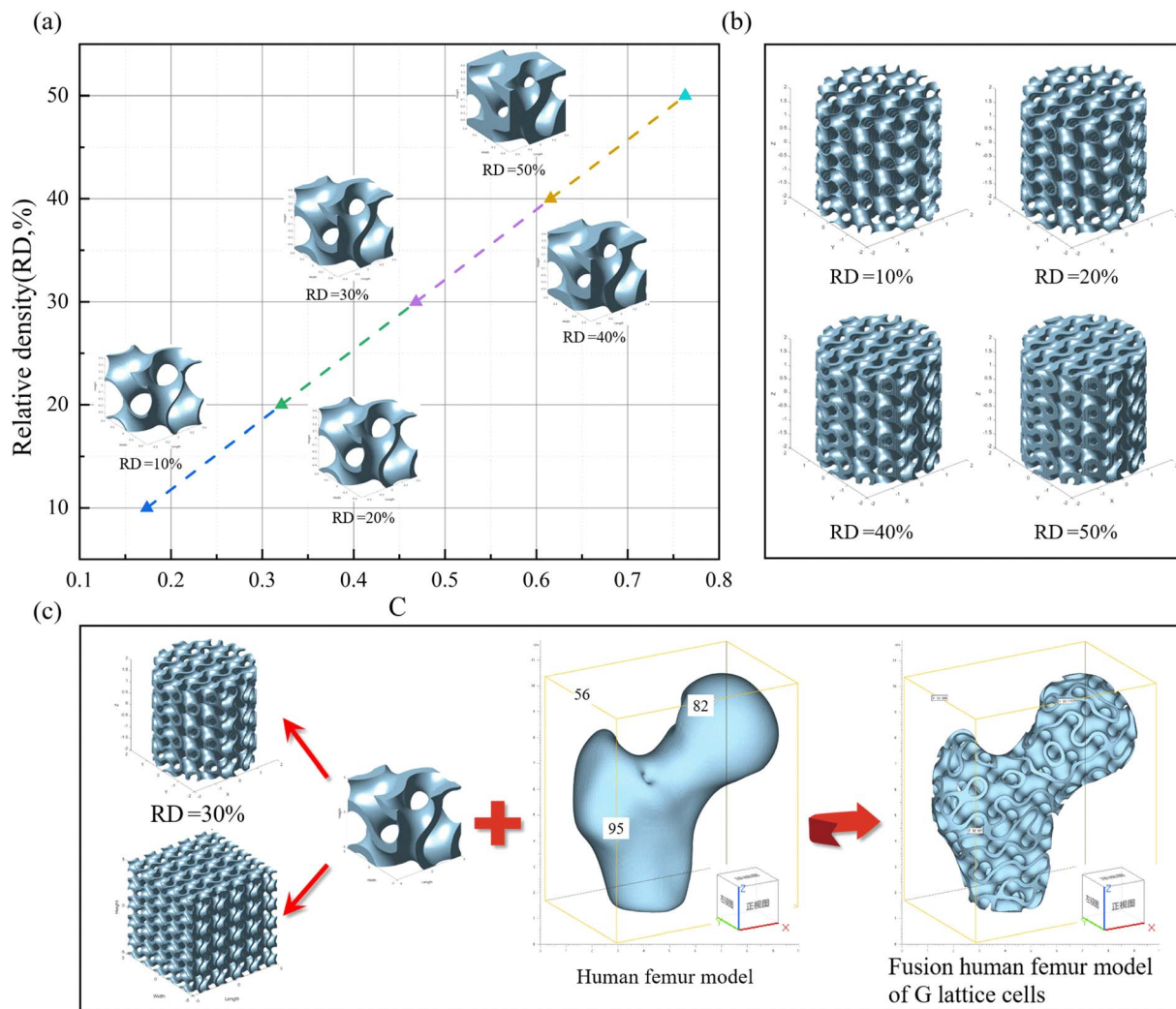


Fig. 1 (a) The relationship between the equation parameter  $C$  of the G TPMS and the corresponding relative density (RD) of the lattice unit cells. There is a positive correlation between RD and  $C$ . It is measured that as the relative density changes from 10% to 50%, the corresponding thickness ( $t$ ) of the G lattice increases from 0.0288 mm to 0.1158 mm; (b) cylindrical model corresponding to RD values ( $\phi$  4 mm diameter, 4 mm high). Observing the cylindrical model, it was found that the porosity of the model gradually decreased as the RD value increased. The theoretical porosity decreased from 90% to 50%; (c) schematics of scaffolds of different structural types constructed based on G lattice cells.

the fundamental unit. The G TPMS with an RD of 30% was selected as the filling lattice, and after merging with the human femur, a porous scaffold model was formed. Therefore, scaffolds with different porosities were constructed based on the Gyroid TPMS lattice structure, and PCL/TM composite scaffolds were fabricated using SLS technology.

## 2.2 Materials

Polycaprolactone pellets (PCL, Capa 6400; Perstorp, Sweden) with a melting point of 60 °C, a molecular weight of approximately 50 000, and a density of 1.146 g mL<sup>-1</sup> at 25 °C were selected as the base material. After crushing and sieving (300 mesh), a PCL powder with a relatively uniform average particle

Table 1 Relationship between G TPMS strut thickness ( $t$ ) and lattice structure characteristics (relative density and surface-to-volume ratio)

$t$ (mm)	Relative density (%)	Surface area (mm <sup>2</sup> )	Volume (mm <sup>3</sup> )	Surface-to-volume ratio (S/V)
0.0288	10	5.16	0.0748	68.98 ± 0.1
0.0549	20	5.49	0.1529	35.91 ± 0.1
0.0775	30	5.78	0.2301	25.12 ± 0.1
0.0979	40	6.01	0.3064	19.61 ± 0.1
0.1158	50	6.16	0.3802	16.20 ± 0.1

size was obtained. Tourmaline (TM, 10 000 meshes) was purchased from Jingwei Mineral Products Processing Plant, Lingshou County, Hebei Province. Sodium stearate ( $C_{17}H_{35}COONa$ , analytical purity) was purchased from Wuxi Yatai United Chemical Co. Phosphate buffer solution (PBS, pH = 7.4) was used as the degradation medium and modified simulated body fluid (SBF, pH = 7.4) was used as the solution for *in vitro* mineralization, both of them were purchased from Fuzhou Feixing Biotechnology Co.

### 2.3 TM modification and PCL/TM powder preparation

An appropriate amount of sodium stearate (1 wt% of the dry material) and a certain amount of distilled water are mixed in a thermostatic water bath. The TM powder is added to the solution and stirred for 25 minutes using magnetic stirring in a water bath at 40 °C. The mixture is then subjected to solid-liquid separation using a centrifuge, followed by washing with anhydrous ethanol at least 3 times to remove residual sodium stearate. The modified TM powder (MTM) and unmodified TM powder (UTM) are obtained after drying (as shown in Fig. 2a). Next, the composite powder is weighed using an electronic balance. The detailed components of each composite powder were shown in Table 2. The preparation process is as follows:

Table 2 The composition of each composite powder

Serial number	Composite powder	PCL content	TM content
1	Pure PCL	100	0.0
2	PCL/1% UTM	99	1
3	PCL/2% UTM	98	2
4	PCL/3% UTM	97	3
5	PCL/4% UTM	96	4
6	PCL/5% UTM	95	5
7	PCL/1% MTM	99	1
8	PCL/2% MTM	98	2
9	PCL/3% MTM	97	3
10	PCL/4% MTM	96	4
11	PCL/5% MTM	95	5

the weighed PCL powder is transferred to a beaker containing anhydrous ethanol and stirred magnetically for 30 minutes to obtain a uniform suspension. The same method is applied to process the TM powder, and the TM suspension is gradually added drop by drop into the PCL suspension, followed by continued magnetic stirring for 30 minutes to obtain a homogeneous PCL/TM suspension. The mixed suspension is then placed in a high-speed centrifuge (8000 rpm) and centrifuged for 10 minutes to separate the supernatant. The damp

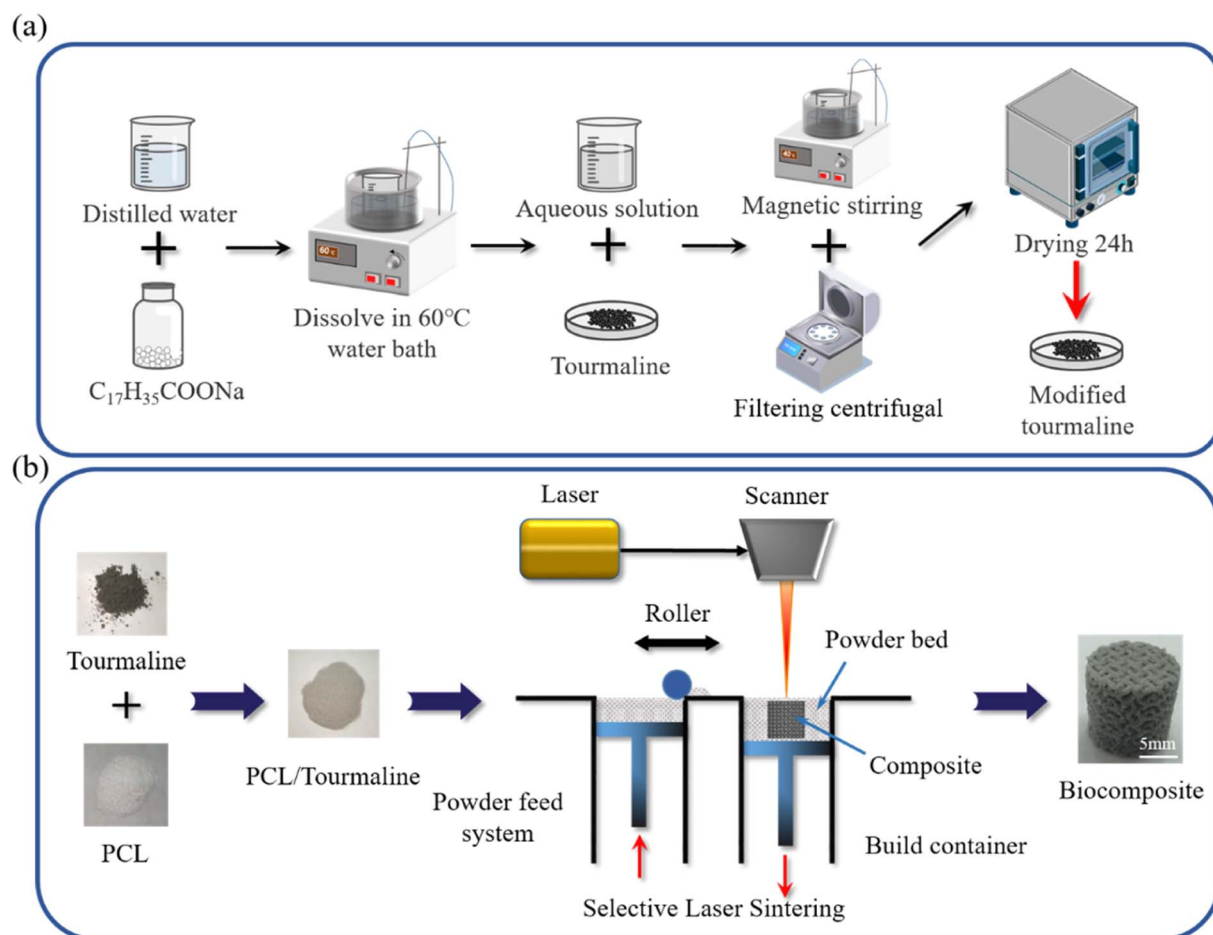


Fig. 2 (a) Schematic diagram of MTM preparation; (b) PCL/TM scaffolds with different contents were prepared by selective laser sintering.





composite powder is removed and dried in a thermostatic drying oven at 45 °C until a constant weight is reached. Finally, mechanical grinding and sieving are performed to obtain the composite powder suitable for SLS processing. These mixed powders were named PCL/1% UTM, PCL/2% UTM, PCL/3% UTM, PCL/4% UTM, PCL/5% UTM and PCL/1% MTM, PCL/2% MTM, PCL/3% MTM, PCL/4% MTM, PCL/5% MTM.

## 2.4 Fabrication of PCL/TM scaffold

The composite scaffolds were prepared using an SLS system built in-house by the group, and the preparation diagram is shown in Fig. 2b. Specifically, the MS Lattice was designed to generate G models with different relative density values into the SLS equipment. Then the infrared laser beam was computer-controlled to sinter the composite powder layer by layer using the appropriate power, speed, and line spacing. The following constant processing parameters were used during the process: laser power: 6 W; laser rate: 1400 mm s<sup>-1</sup>; layered thickness: 0.15 mm; laser scan pitch: 0.15 mm. The size of the porous holder was a cylindrical specimen of  $\Phi$  10 mm  $\times$  10 mm. The size of the tensile part follows the standard GB/T 16421-1996 "Test Method for Small Specimens of Tensile Properties of Plastics" and measures 37.5 mm in length, 2.5 mm in width at the middle section, and 4 mm in thickness for a bone-shaped specimen.

## 2.5 Characterization

The TM's morphology before and after modification was observed by scanning electron microscopy (SEM, Phenom ProX, Phenom-World BV, Eindhoven, Netherlands). The crystal structure of TM was examined using X-ray diffraction (XRD, AL-2700B, Dandong Aolong Ray Instrument Co., Ltd, China) at a scanning speed of 4° min<sup>-1</sup> over a  $2\theta$  range of 10°–70°, with an X-ray tube voltage of 40 kV and a current of 30 mA. The chemical groups on the MTM surface were studied using Fourier Transform Infrared Spectrometer (FTIR, NicoletteTM 6700, Thermo Scientific IN10, USA). The dispersion of TM in the composite support was observed using SEM, and its elemental composition and distribution were analyzed by Energy Dispersive Spectrometer (EDS). Before SEM analysis, all samples were subjected to gold sputter coating (10 mA, 120 s) to enhance conductivity. Compression and tensile tests were performed by the Universal Testing Machine (ZQ-990LA, Dongguan Wisdom Precision Instruments Co.). The tensile and compressive properties of the standard tensile and compressive samples were tested at a strain rate of 1 mm min<sup>-1</sup>, with no less than three sets of test data.

## 2.6 Degradation performance

The scaffolds were immersed in PBS solution (pH = 7.4, 37 °C) for 28 days to study the biodegradability of the scaffolds, characterized in terms of mass loss, change in pH, and microscopic morphology before and after degradation. Weigh all the scaffolds to be immersed using an electronic balance and record as  $M_0$ . The composite scaffolds were separately immersed in different test tubes containing 5 mL of PBS solution at 37 °C.

When the soaking time reached 7, 14, 21, and 28 days, the scaffolds were removed from the solution, with the solution being changed every 2–3 days during the process. Firstly, they were rinsed with distilled water and then blotted with absorbent paper to remove excess water from the surface of the scaffolds. Subsequently, the scaffolds were weighed using an electronic balance and recorded as  $M_1$ . Finally, placing the scaffolds in a vacuum drying oven for 12 hours to a constant weight and removed and weighed as  $M_2$ . Then the water absorption rate can be calculated by eqn (4):

$$\text{Water absorption} = \frac{M_1 - M_0}{M_0} \times 100\% \quad (4)$$

The weight loss rate can be calculated from eqn (5):

$$\text{Weight loss} = \frac{M_0 - M_2}{M_0} \times 100\% \quad (5)$$

The pH of the degradation solution was measured every 7 days during the 28 days of immersion. The microscopic morphology of the scaffold degradation at different immersion times was compared using SEM.

## 2.7 Biomineralization

The biomineralization ability of composite scaffolds at a ratio of 1–5% MTM was investigated by analyzing the formation of an apatite layer on the surface of the scaffold when immersed in SBF, with PCL and 3% UTM scaffolds as control groups. The scaffolds were immersed in SBF at 37 °C for 28 days, and the SBF solution was renewed every 2 days. When the immersion time reached 28 days, samples were removed and rinsed several times with distilled water to remove mineral salts adhering to the surface and then dried at 45 °C for 24 hours to constant weight. SEM and EDS were used to assess the formation of apatite layers on the surface of the scaffolds.

## 2.8 Statistical analysis

Statistical analysis of the quantitative data in this study was expressed as mean  $\pm$  standard deviation. Results One-way ANOVA was used to evaluate the data, which were statistically significant when  $p < 0.05$ , with \* showing  $p < 0.05$  and \*\* indicating  $p < 0.01$ .

# 3 Results and discussion

## 3.1 TM characterization

Fig. 3a and b shows the SEM images of the unmodified and modified TM. Observing the aggregation of UTM in Fig. 3a, it can be noticed that there are numerous smaller-sized UTM particles. As we know, smaller particle size leads to larger surface energy, which makes them more prone to agglomeration. In Fig. 3b, the image of MTM reveals smaller-sized particles as well, but they appear to be more dispersed, indicating the success of the modification process. Fig. 3c(a) and (b) shows the XRD patterns of TM before and after the modification. The



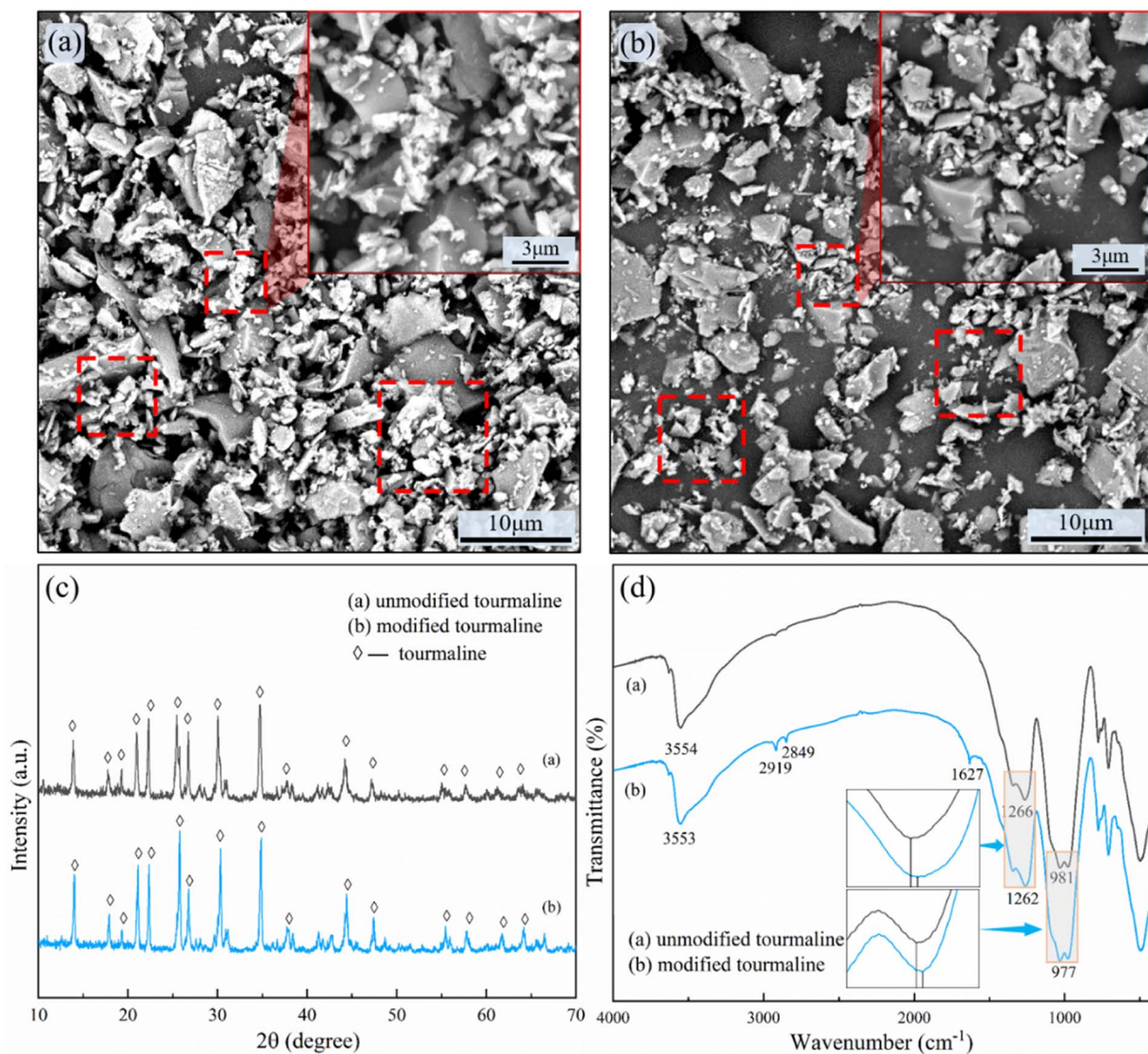


Fig. 3 (a) SEM images of UTM; (b) SEM images of MTM; (c) XRD spectra of TM before and after modification; (d) FTIR spectra of TM before and after modification.

primary peaks of UTM appear at  $2\theta$  angles of  $13.8^\circ$ ,  $17.9^\circ$ ,  $19.3^\circ$ ,  $20.9^\circ$ ,  $22.3^\circ$ ,  $25.5^\circ$ ,  $26.7^\circ$ ,  $30.1^\circ$ ,  $34.7^\circ$ ,  $37.7^\circ$ ,  $44.3^\circ$ ,  $47.1^\circ$ ,  $55.3^\circ$ ,  $57.7^\circ$ ,  $61.7^\circ$  and  $64.1^\circ$ . The primary peak of the MTM was located at a similar  $2\theta$  angle and no other phases were found. A substantial body of research has shown that modification does not alter the crystal structure of TM. For instance, Hu *et al.*<sup>18,19</sup> employed stearic acid modification on TM and characterized the samples using XRD and FTIR. They found that the XRD patterns remained unchanged before and after modification, while FTIR spectra indicated the presence of stearic acid attached to the surface. The FTIR spectra of the TM before and after modification are shown in Fig. 3d. In Fig. 3d(a), the UTM showed absorption bands at  $3568\text{ cm}^{-1}$  (–OH group),  $1276\text{ cm}^{-1}$  (B–O group), and  $983\text{ cm}^{-1}$  (Si–O group). Fig. 3d(b) showed the FTIR spectra of MTM. Apart from the alkyl characteristic peaks at  $2919\text{ cm}^{-1}$  and  $2849\text{ cm}^{-1}$ , and the carbonyl peak at  $1627\text{ cm}^{-1}$ , the characteristic absorption peaks of TM remained

unchanged. Still, the characteristic peaks were all shifted towards the lower wavenumbers by a few wavenumbers compared to UTM, indicating a chemical coupling reaction between sodium stearate and the surface of TM powder, which introduced stearyl groups on the surface of TM.<sup>19,29,30</sup>

### 3.2 Scaffold porosity selection

A common problem encountered in tissue engineering is that cell attachment and proliferation at the outer edges of the scaffold can limit cell penetration into the center of the scaffold, potentially leading to the formation of a necrotic cavity in the center.<sup>4</sup> This can be done by optimizing the scaffold to improve nutrient and cell penetration into the center of the scaffold, commonly by improving the pore size and porosity of the scaffold. In this paper, porous bone scaffolds with different porosity were designed and generated using SLS preparations of MS Lattice. To determine the suitable porosity, the scaffold's



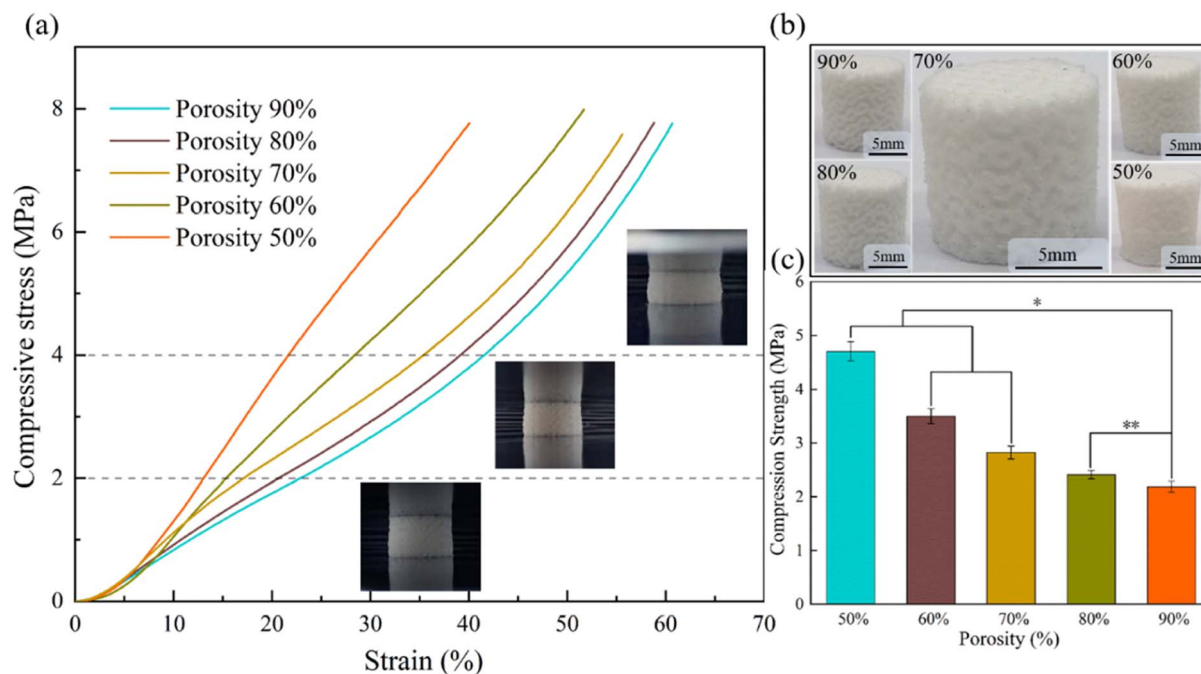


Fig. 4 (a) Comparison of compression performance of different porosity; (b) macroscopic surface morphology of pure PCL scaffolds with varying porosities; (c) stress magnitude at 25% strain. \* Represents statistical difference (\* $p < 0.05$ , \*\* $p < 0.01$  when compared with the PCL scaffold with a porosity of 90%).

surface was observed, and its compression performance was tested. Based on these observations and tests, the appropriate porosity was selected. Scaffolds with 90–50% porosity prepared using SLS are shown in Fig. 4b. The surface porosity is visible in the scaffolds with porosities of 90% and 80%. For the scaffold with a porosity of 70%, the surface pores are visible. In the case of a 60% porosity scaffold, most of the surface pores are blocked. However, for the scaffold with a porosity of 50%, the surface pores are nearly imperceptible. Tissue engineering scaffolds require sufficient porosity to ensure permeability, allowing fluid (e.g. nutrients) to circulate through the scaffold.<sup>31</sup> Therefore, we have preliminarily chosen a porous scaffold with a porosity ranging from 90% to 70% as our optional scheme.

As the bone scaffold is implanted in the area of the bone defect, it needs to support the weight together with the human bone and to protect and support other tissues. Therefore, the bone scaffold is always under a certain stress field and needs to have a certain mechanical strength.<sup>32</sup> Fig. 4a shows the stress-strain curves for brackets with different porosities. It is clear that as the porosity decreases, the compressive capacity of the scaffold gradually increases and the slope of the stress-strain curve increases the compressive modulus. The diagram shows the compression of the scaffold at the corresponding strain. As the scaffold was not damaged during the compression experiments, the stress at a strain of 25% is chosen here as its compressive strength according to GBT 1041-1992 (Fig. 4c), and it can be seen that the compressive strength of the scaffold with 70% porosity is  $2.8 \text{ MPa} \pm 0.1 \text{ MPa}$ , and the maximum compressive strength of the scaffold with 50% porosity is  $4.7 \text{ MPa} \pm 0.3 \text{ MPa}$ . This is comparable to natural cancellous

bone, exhibiting a compressive strength of 2–12 MPa.<sup>33</sup> Thus, the tested scaffolds fall within the range of compressive capacity. After thorough consideration, a porous structure with a porosity of 70% was selected as the optimal design for subsequent printing of composite materials.

### 3.3 Mechanical properties of the scaffold

Based on the stress-strain curves depicted in Fig. 5a, it is evident that the inclusion of UTM leads to an increase in tensile strength, while the elongation at break exhibits slight variation at different proportions. In Fig. 5b, the ultimate tensile stresses of the stents with varying UTM contents are depicted. At a 2% UTM content, the maximum ultimate tensile stress reaches 3.6 MPa, representing an improvement compared to PCL. Fig. 5c illustrates the tensile modulus of the UTM scaffolds at different proportions, showing an improvement compared to PCL. Moving on to Fig. 5d displays the stress-strain curve for the MTM sample. At an MTM content of 3%, the maximum ultimate tensile stress reaches 3.9 MPa, representing a 21.4% increase compared to the 3.2 MPa of the PCL sample. The elongation at break consistently decreases as the MTM content increases. Fig. 5e demonstrates the ultimate tensile stresses of the UTM supports, which exhibit a significant improvement compared to PCL. Similarly, Fig. 5f presents the tensile modulus for various proportions of MTM, following the same trend as the tensile stress and reaching a maximum value of 38.6 MPa at a 3% MTM content. It is noteworthy that the best tensile properties are achieved at a TM content of 2% before modification and 3% after modification. This indicates that TM modification positively affects the tensile properties, thus





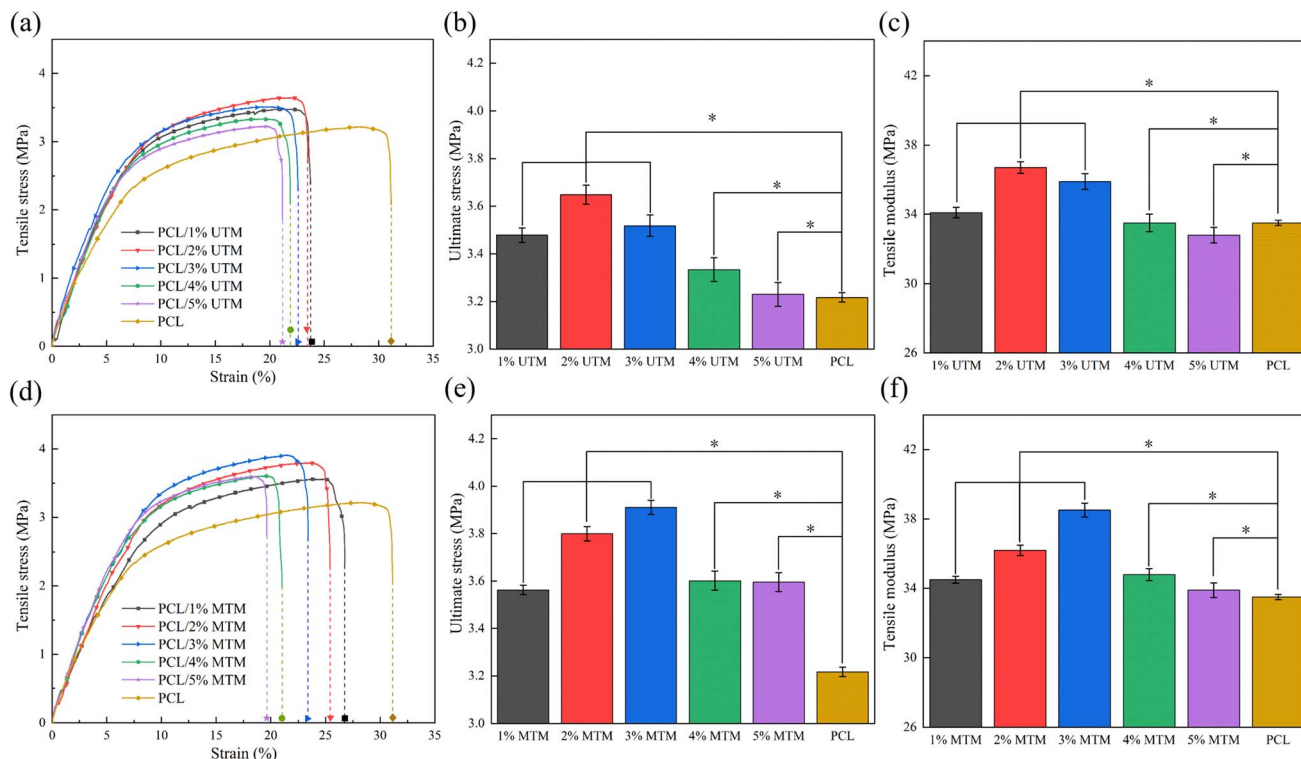


Fig. 5 (a) PCL/UTM samples tensile stress–strain curve; (b) ultimate stress and (c) tensile modulus of UTM sample; (d) PCL/MTM samples tensile stress–strain curve; (e) ultimate stress and (f) tensile modulus of MTM sample. \* Represents statistical difference ( $p < 0.05$ ,  $p < 0.01$  when compared with the PCL scaffold).

serving as an effective approach to further enhance the composite's performance.

To evaluate the effect of TM on the mechanical properties of composite scaffold, the compression resistance of each scaffold was evaluated by compression tests, and the results were shown in Fig. 6. Among them, the PCL scaffold with a porosity of 70% was set as a control group to better judge the role of TM in mechanical enhancement. Fig. 6a shows the stress–strain curve for the PCL/UTM scaffold, comparing the magnitude of stress at 25% strain, as shown in the bar graph in Fig. 6a. The stress–strain curve for the PCL/MTM scaffold is shown in Fig. 6c and has a similar trend to the UTM, with the composite scaffold showing an increasing trend in compressive stress below 3% content, reaching a maximum at both 3%. Fig. 6d presents the comparison of compressive stress at 25% strain before and after TM modification. At 25% strain, the compressive stress of the 3% UTM scaffold is 3.4 MPa, which is 21.4% higher than the pure PCL scaffold with a compressive stress of 2.8 MPa. The 3% MTM scaffold exhibits a compressive stress of 3.7 MPa, representing a 32.1% increase compared to the pure PCL scaffold. Regrettably, when the content of UTM continued to increase, the strength of the composite scaffold was found to decrease instead. This may be because the lower content of TM powder is homogeneously dispersed in the polymer matrix and acts as an axial reinforcement, enhancing the compressive strength of the polymer. When the content exceeds 3%, there is an increased probability of agglomeration within the polymer matrix, even with modification. This agglomeration tends to result in stress

concentration and a subsequent reduction in mechanical performance.

### 3.4 SEM microscopic morphological observations

The surface morphology of composite scaffolds with different ratios was observed using SEM, and the results are shown in Fig. 7. TM powder exhibits a sandwich-like structure within the PCL matrix, with no distinct interface between TM and the PCL matrix, indicating good compatibility and effective dispersion of TM within the matrix. The colored boxes in Fig. 7 represent zoomed-in views of specific regions, and the yellow box corresponds to a similar phenomenon. Fig. 7a shows the surface morphology of a pure PCL scaffold, which appears smooth and flat. Fig. 7b and c demonstrate well-dispersed UTM content at 1% and 2%. However, when the UTM content reaches 3% (Fig. 7d), significant agglomeration occurs in the central region of the image. At UTM mass fractions exceeding 3% (Fig. 7e and f), severe agglomeration is observed within the PCL matrix. Fig. 7g–k display the surface morphology of MTM composite scaffolds with contents ranging from 1 wt% to 5 wt%. It is observed that MTM content at 1%, 2%, and 3% shows good dispersion and uniform distribution within the PCL matrix. However, at 4% MTM mass fraction, slight agglomeration occurs within the PCL matrix. At a content of 5%, agglomeration becomes more pronounced (Fig. 7k). These observations can be explained as follows: this is because the organic groups on the surface of the MTM powder are lipophilic when the MTM





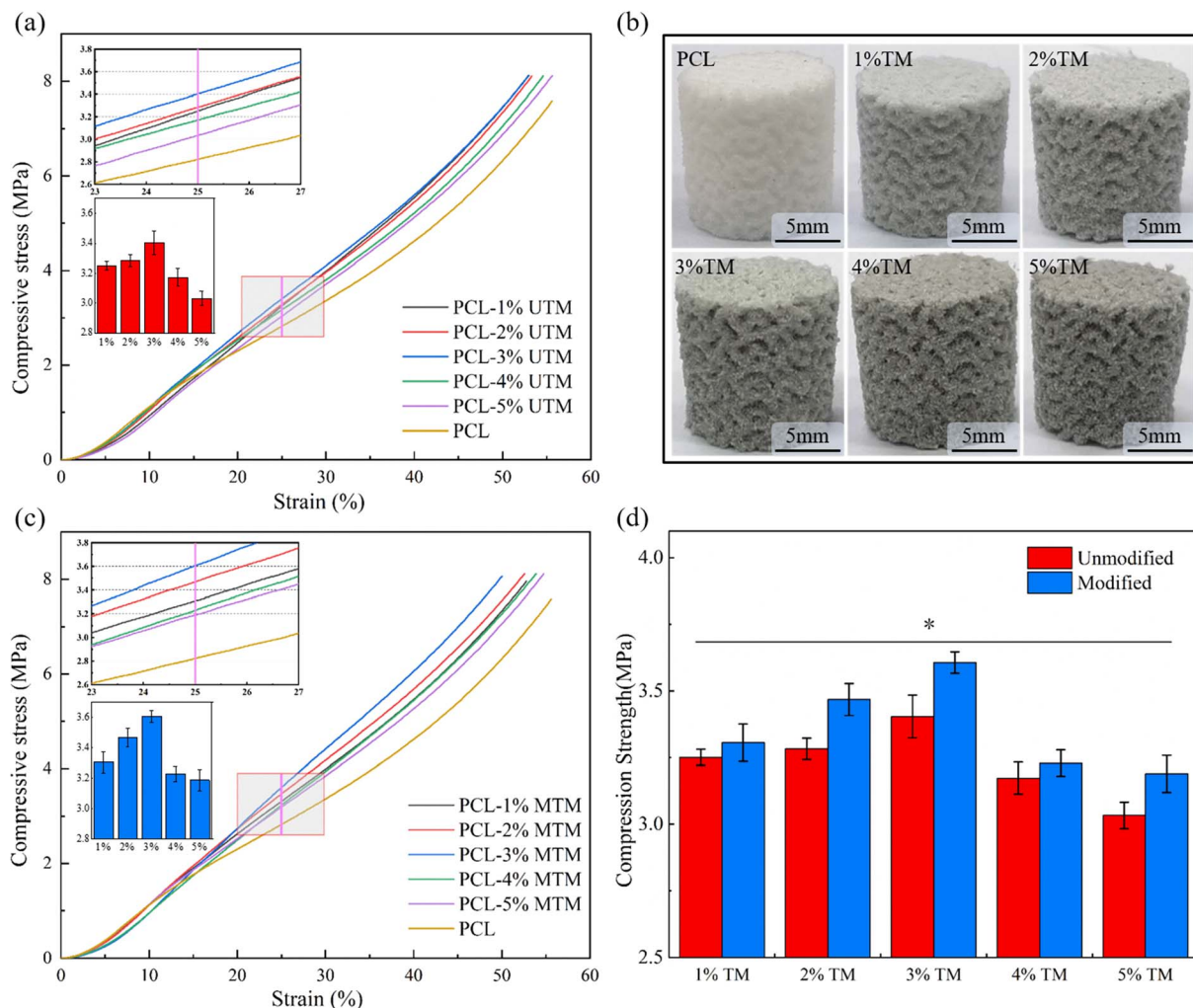
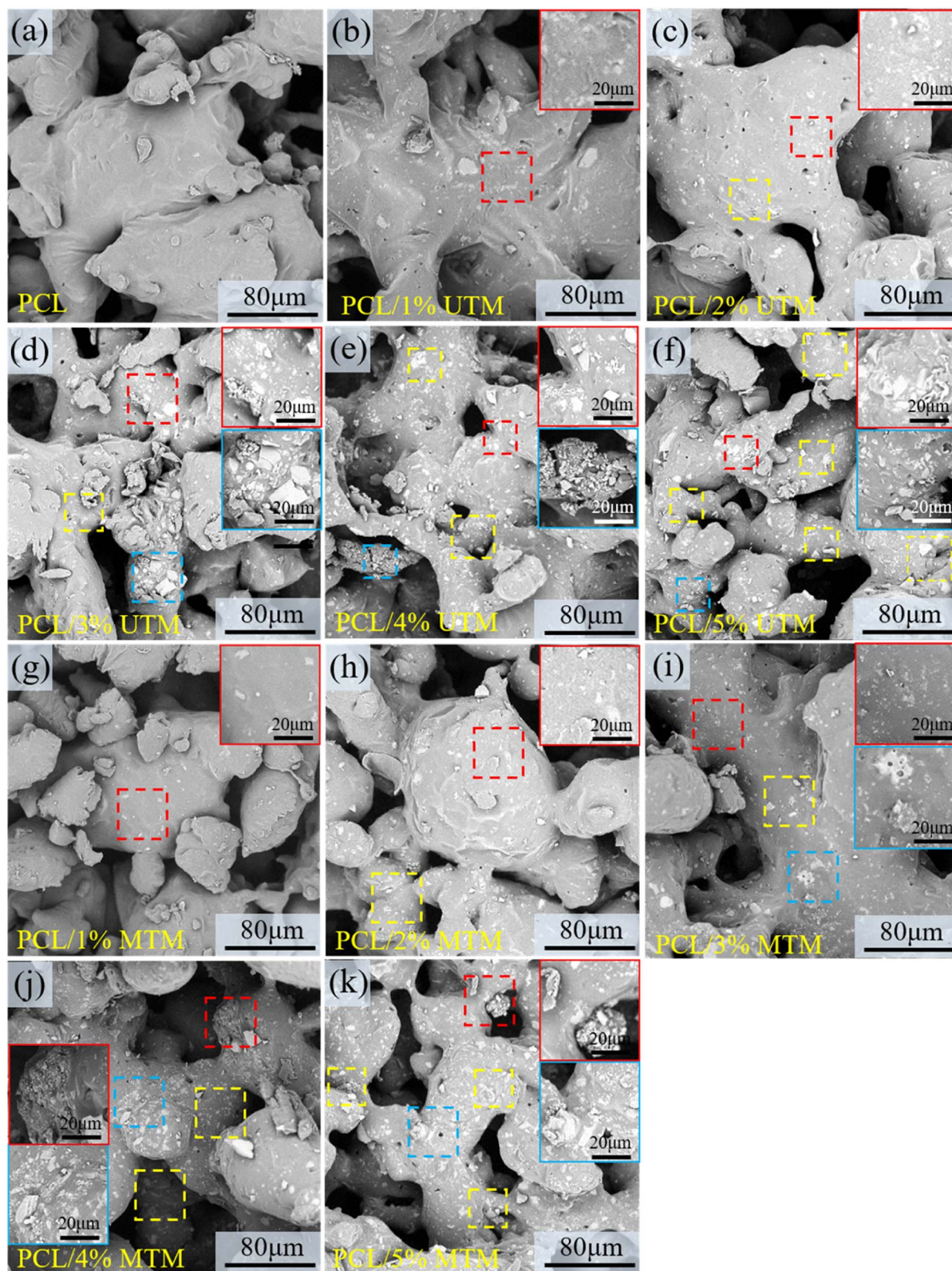


Fig. 6 (a) PCL/UTM scaffold compression stress–strain curve; (b) composite scaffold with a porosity of 70%; (c) PCL/MTM scaffold compression stress–strain curve; (d) comparison of compression stress before and after TM modification at 25% strain. \* Represents statistical difference ( $p < 0.05$ ,  $**p < 0.01$  when compared with the PCL scaffold).

addition is small, while the hydrophobic long chains make the MTM more easily dispersed and have good compatibility with the PCL material. However, agglomeration occurs in the matrix when the powder mass fraction is too large due to the enhanced interaction between nanoscale second-phase particles during the co-mingling process.<sup>34</sup>

The tensile fracture surface of the samples was observed using SEM. The colored boxes in Fig. 8 represent zoomed-in views of specific regions, and the red arrow corresponds to a similar phenomenon. The pure PCL tensile specimen has a large number of slender tensile ligaments at fracture, and the elongation at break is high. In Fig. 8b, numerous elongated and thin ligaments can be observed. In Fig. 8c, there are fewer short and thin ligaments, and some ligaments start to thicken. In Fig. 8d, thicker ligaments can be observed, and there is a small accumulation of UTM at the fracture site. In Fig. 8e and f, when the UTM content is excessively high, there are significantly fewer elongated stretching bands within the field of view, and UTM detachment with the formation of indentations can be

observed at the fracture surface. Fig. 8g shows a digital photograph of the macroscopic morphology of a partial tensile specimen after a tensile fracture. At an MTM content of 1–2% (Fig. 8h and i), the elongated ligaments are distributed throughout, exhibiting good elongation properties. As the content of MTM increases, it can also be seen that the elongation of the tensile ligament at the break decreases. When the MTM content was 3% (Fig. 8j), there were a large number of thick tensile ligaments in the field of view, and MTM was evenly dispersed in it, and shedding was rarely seen. However, when the MTM content increases to 4% and 5%, localized aggregation, and detachment are observed at the fracture surface (Fig. 8k and l). This phenomenon can lead to the occurrence of detachment and indentation in high-proportion tensile samples during the stretching process, resulting in a decrease in tensile strength. Therefore, it can be inferred that as the TM content increases, the occurrence of aggregation and detachment may have a negative impact on the mechanical properties of the material.



**Fig. 7** The surface morphology of composite scaffolds with different ratios was observed using SEM (a–k). Upon observing the surface of the scaffold, at lower contents, UTM can be uniformly dispersed within the matrix. However, at a content of 3%, aggregation is already evident. MTM demonstrates better dispersion than UTM, with aggregation occurring only when the MTM content exceeds 4%. Indeed, the higher surface polarity of UTM makes it more prone to aggregation within the polymer matrix. On the other hand, the modification of MTM reduces its surface polarity, resulting in a decrease in the occurrence of aggregation.





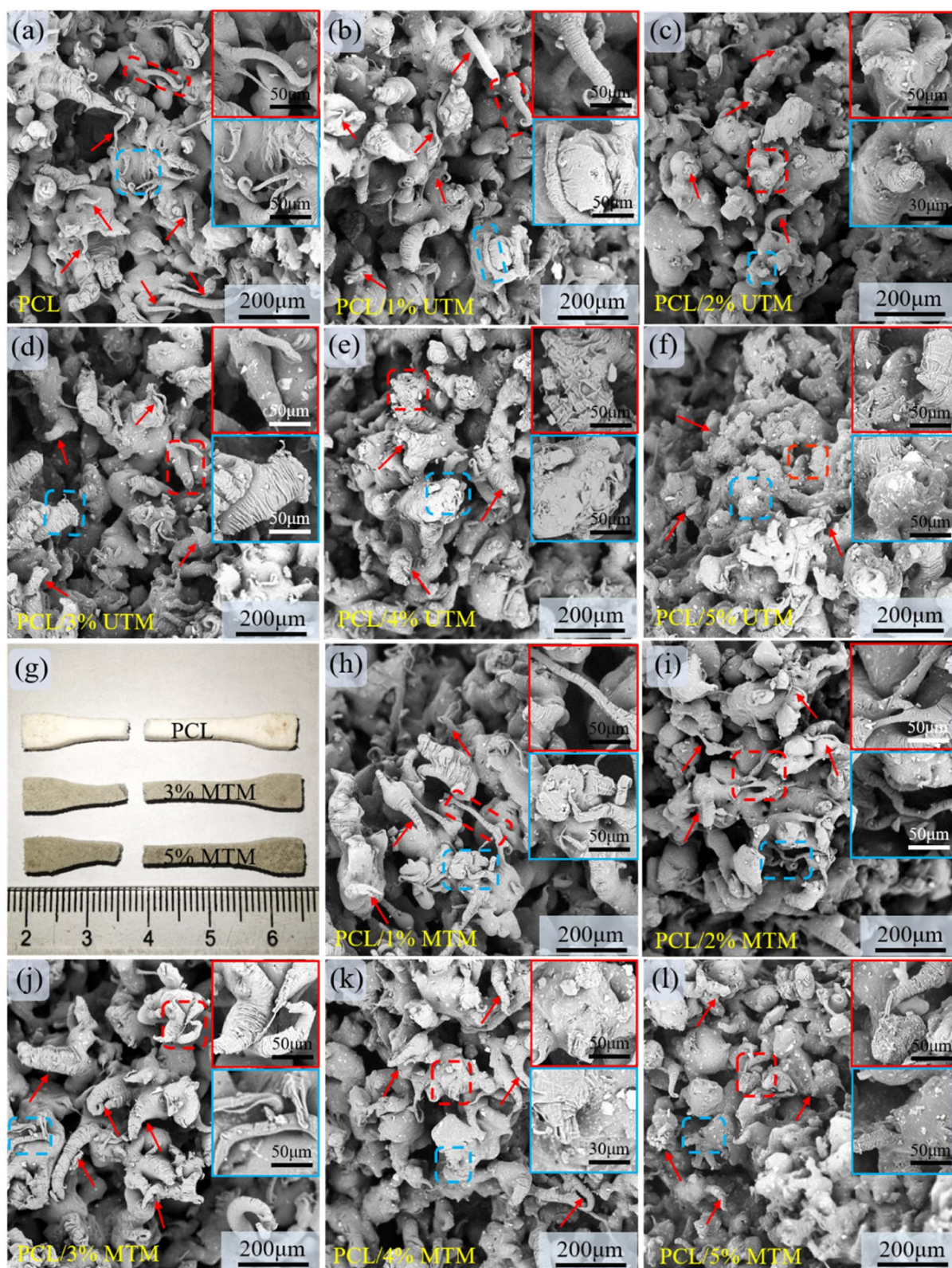
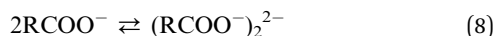
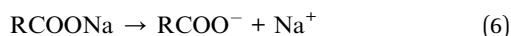


**Fig. 8** SEM micrographs of the cross-sections of the tensile samples at various content (a–l). This figure provides a visual comparison showing the transformation of elongated ligaments into shorter and thicker ligaments as the TM content increases. However, when the TM content exceeds 3%, there is evidence of agglomeration at the fracture site, accompanied by detachment and the formation of voids. This leads to stress concentration, resulting in a decrease in tensile stress.



### 3.5 Modifiers and TM surface mechanisms

Fig. 9 shows the possible adsorption mechanism of sodium stearate on the TM surface. The UTM surface was covered with hydroxyl groups and the active center of the surface was present with  $\text{Ca}^{2+}$ ,  $\text{Fe}^{2+}$ , and  $\text{Mg}^{2+}$  ions. The organic modifier sodium stearate is then added and formulated into a suspension. The organic carboxylate ( $\text{RCOOMe}$ , Me is the metal ion) first dissociates in an aqueous solution and generates an organic carboxylic acid ion ( $\text{RCOO}^-$ ), then  $\text{RCOO}^-$  is hydrolyzed to produce the organic carboxylic acid  $\text{RCOOH}$  by the following chemical reaction:<sup>35</sup>



The main components involved in this process are  $\text{RCOO}^-$  and  $\text{RCOOH}$ . Through mixing and stirring,  $\text{RCOO}^-$  ions adsorb onto the surface metal ions, while  $\text{RCOOH}$  adsorbs onto the hydroxyl groups due to hydrogen bonding. The strong adsorption between the modifier and the TM contributes to the above-mentioned good modification effect.<sup>36,37</sup> Additionally, during the SLS manufacturing process, the enhanced dispersion of the MTM in PCL can result in the formation of more hydrogen bonds, leading to a significant improvement in the mechanical properties of the material compared to before modification.

### 3.6 Degradation morphology analysis

Polycaprolactone (PCL) is a hydrophobic material with low hydrophilicity, so it is often blended with other hydrophilic materials. In this study, TM was used as a hydrophilic material and mixed with PCL to improve the overall properties of the composite material.<sup>38</sup> To evaluate the effect of TM modification on scaffold degradation, a PCL/3% UTM composition was chosen as a control for comparison with the MTM samples.

The initial weight of the scaffolds was recorded, and their weight loss was measured every 7 days (Fig. 10a). The pH of the solution (Fig. 10b) and water absorption (Fig. 10c) were also monitored. As shown in Fig. 10a, after 28 days of immersion, the pure PCL scaffold exhibited the lowest weight loss, which slightly increased with the addition of TM, reaching approximately 1.5% for all compositions. During degradation, PCL releases acidic by-products, leading to a gradual decrease in the pH of the solution over time (Fig. 10b). The initial pH of the PBS solution was 7.4, and after 28 days, the pH of each composition was around 7.1, similar to the reported extent of PCL degradation.<sup>39</sup>

Notably, the scaffolds exhibited significantly higher water uptake compared to the pure PCL scaffold (Fig. 10c). The pure PCL scaffold showed the lowest water absorption, while the water absorption gradually increased with increasing MTM content. When the MTM content reached 5%, the water absorption peaked at around 7%. Because the TM surface contains abundant hydroxyl groups, which are hydrophilic in nature. These hydroxyl groups enhance the water absorption capacity of the scaffold, thereby accelerating its degradation

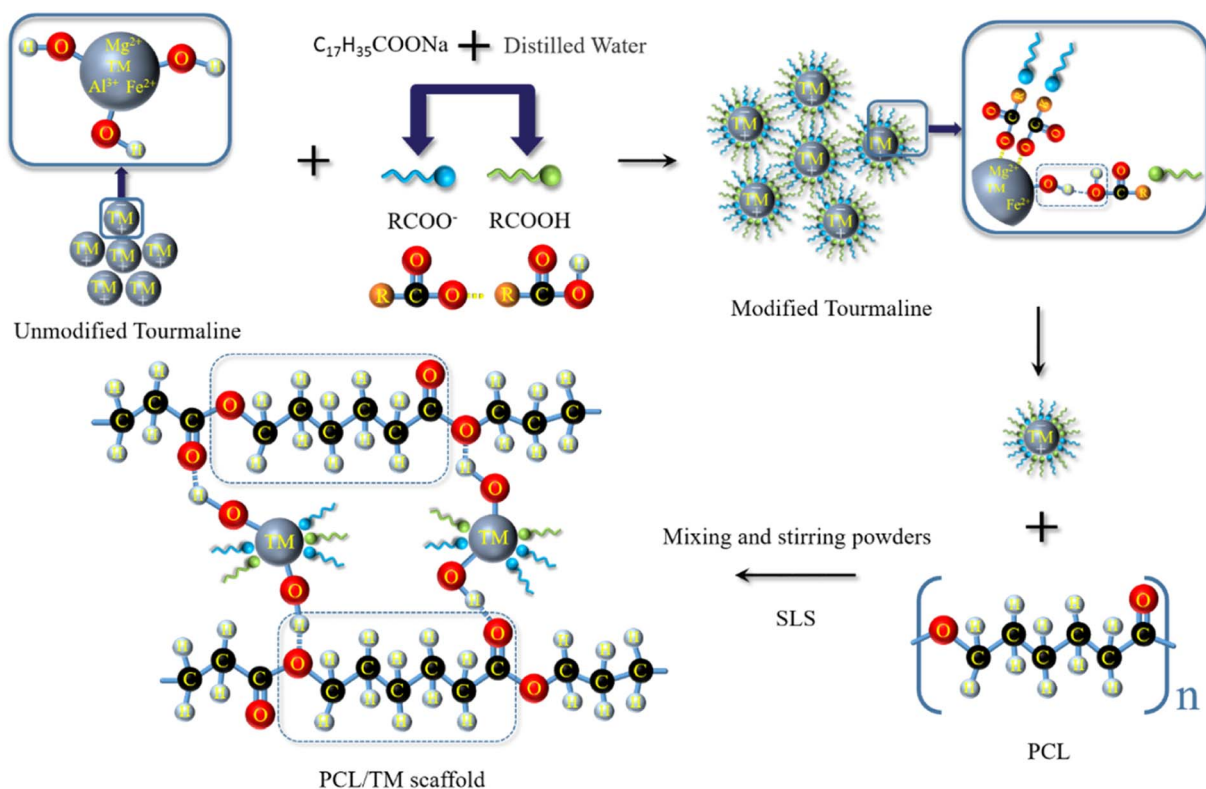


Fig. 9 Mechanism of action of sodium stearate on TM modification.



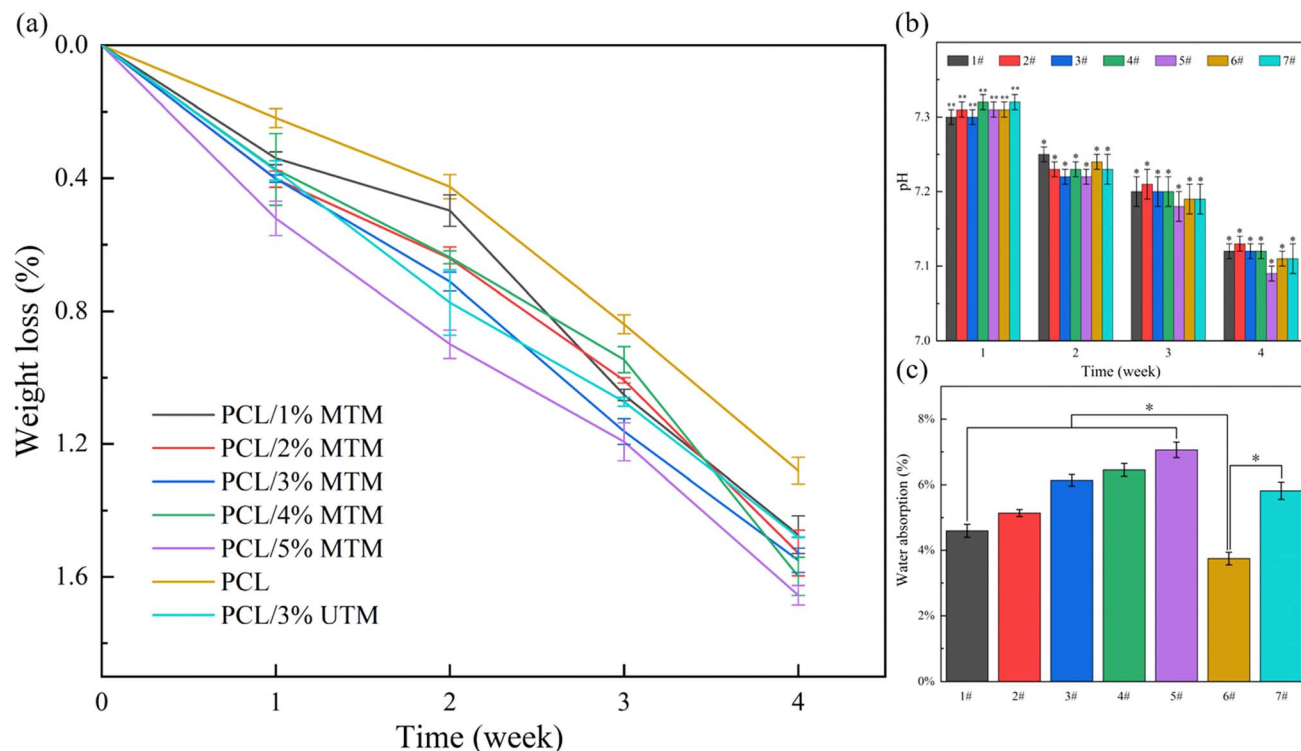


Fig. 10 (a) Weight loss of the scaffolds; (b) pH of the solution; (c) water absorption. 1# represent the PCL/1% MTM scaffold, 2# represent the PCL/2% MTM scaffold, 3# represents the PCL/3% MTM scaffold, 4# represents the PCL/4% MTM scaffold, 5# represents the PCL/5% MTM scaffold, 6# represents the PCL scaffold, 7# represents the PCL/3% UTM scaffold. \* Represents statistical difference ( $p < 0.05$ ,  $**p < 0.01$  when compared with the PCL scaffold).

process. Water absorption is an important factor for bone scaffolds as it reflects the ability to absorb fluids and deliver nutrients efficiently. The water absorption of the 3% UTM

scaffold and the 3% MTM scaffold was similar, indicating that TM modification had a minimal impact on the water absorption of the scaffold.

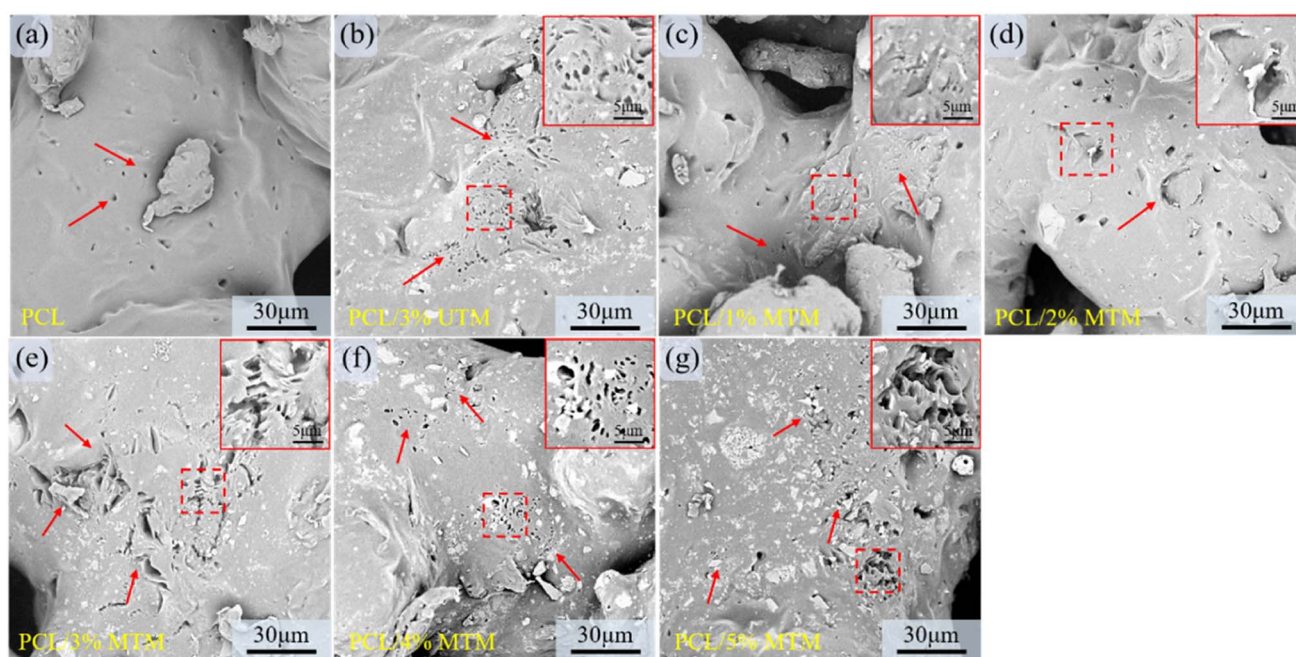


Fig. 11 After immersing in PBS for 4 weeks, the surface morphology of PCL and composite scaffolds was observed (a–g). Scaffolds with lower MTM content only show a few small pores on the surface, while PCL/3% MTM, PCL/4% MTM, and PCL/5% MTM scaffolds exhibit large areas of pore formation and collapse within the field of view. This makes it easier for the solution to penetrate the interior and promote degradation.



The surface morphology of the composite scaffolds after 28 days of immersion in PBS is shown in Fig. 11. In Fig. 11a, the surface of the PCL scaffold exhibits slight degradation, with only a few small micropores present. In contrast, the PCL/3% UTM scaffold shows localized micropores and small cracks on its smooth surface (Fig. 11b). Upon closer observation of the surfaces of the PCL/1% MTM and PCL/2% MTM scaffolds (Fig. 11c and d), they appear rougher with the presence of fine micropores. In Fig. 11e, the PCL/3% MTM scaffold exhibits large area pore formation and collapse within the field of view, allowing the solution to penetrate the interior more easily and promoting degradation. Similar observations are made for the

PCL/4% MTM and PCL/5% MTM scaffolds (Fig. 11f and g), where large pore formations are observed on the outer surface as well.

Upon referring back to Fig. 10a, at the 4-week mark, there are slight differences in the weight loss among the scaffolds with different ratios. Scaffolds with a higher MTM content exhibit a higher degree of weight loss due to the appearance of cracks on the degradation surface, which facilitates the penetration of liquids into the scaffold's interior. The above observations indicate that whether TM is modified or not does not have a significant impact on the degradation of the composite scaffold.

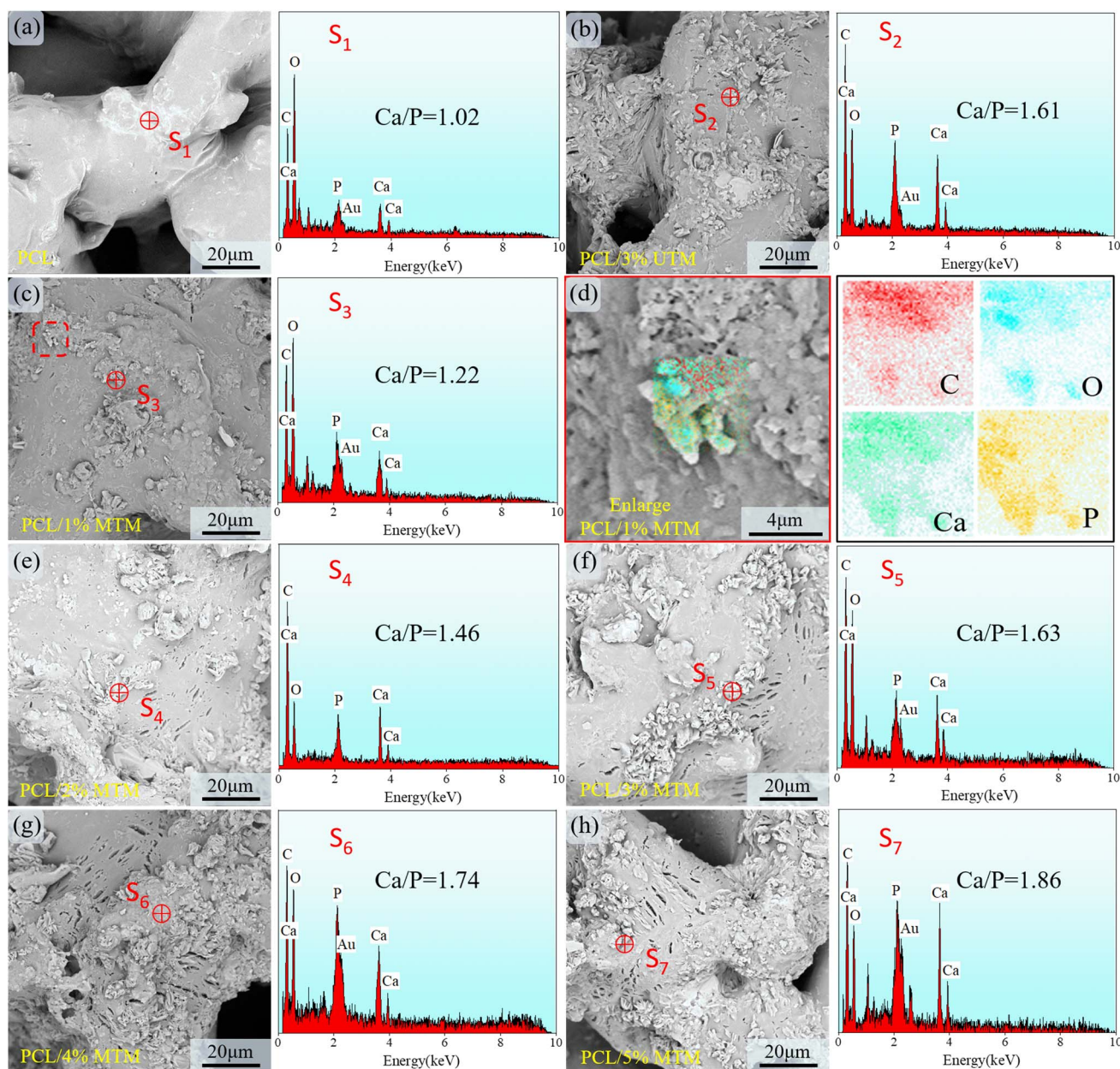


Fig. 12 SEM micrographs of the scaffolds incubated in SBF solution for 28 days and corresponding EDS spectra (magnification  $\times 2000$ ). (a) The PCL scaffold, (b) the PCL/3% UTM scaffold, (c) the PCL/1% MTM scaffold, (d) local face sweep of PCL/1% MTM scaffold, (e) the PCL/2% MTM scaffold, (f) the PCL/3% MTM scaffold, (g) the PCL/4% MTM scaffold, (h) the PCL/5% MTM scaffold.





### 3.7 Biomineralization assessment

The ion concentrations in simulated body fluid (SBF) closely resemble those found in human blood. The prepared scaffold is immersed in SBF to assess its ability to form a bone-like apatite on the surface, which serves as an indicator of the scaffold's bioactivity. After 28 days of immersion, the surface morphology of the scaffolds was examined, and the results are shown in Fig. 12. Fig. 12a shows the PCL scaffold, where a faint gray band can be observed on the originally smooth surface. EDS analysis at point S1 reveals the presence of calcium (Ca) and phosphorus (P) elements, with a Ca/P ratio of approximately 1.02, indicating a low bioactivity of the PCL scaffold. In contrast, numerous deposits of bone-like apatite were observed on the surface of the 3% UTM scaffold (Fig. 12b), and EDS analysis yielded a Ca/P ratio of approximately 1.61. In Fig. 12c, surface scanning of the PCL/1% MTM scaffold revealed the presence of Ca and P elements within the localized region, further confirming the presence of apatite deposits (Fig. 12d). As the MTM proportion increased, as shown in Fig. 12e and f, the deposition of apatite on the surfaces of the PCL/2% MTM and PCL/3% MTM scaffolds became more evident, with Ca/P ratios of approximately 1.46 and 1.63, closely resembling the ratio of natural hydroxy-apatite. When the MTM proportion reached 4% and 5% (Fig. 12g and h), the phenomenon of apatite deposition was observed throughout the field of view, with Ca/P ratios of approximately 1.74 and 1.86. Liang Jinsheng *et al.* added TM to the polymer composite membrane and found that an electrostatic field existed around the TM particles, which could electrolyze part of the water when it was in contact with water and could adjust the pH of the solution to be more conducive to the production of HA.<sup>14,40</sup> These results suggest that PCL/TM scaffolds exhibit good bioactivity and have the potential to induce new bone formation after implantation.

## 4 Conclusions

In summary, this study has designed a porous bone scaffold model using the triply periodic minimal surfaces (TPMS), followed by the fabrication of the scaffold using selective laser sintering (SLS) technology, followed by the fabrication of the scaffold using selective laser sintering (SLS) technology. The main work of this study is as follows: TM was modified with sodium stearate and PCL/TM composite scaffold was successfully prepared through SLS. The results showed that the dispersibility of MTM was significantly improved, while the FTIR spectra showed that the stearyl group was successfully grafted onto the TM surface. The mechanism can be explained by the dissociation of sodium stearate from RCOO<sup>−</sup> and RCOOH in solution, which are adsorbed on the TM surface through ionic and hydrogen bonds, and the hydrophobic long chains allow for better TM dispersion. In addition, the mechanical properties of PCL/TM scaffolds improved significantly with the incorporation of TM and reaching a tensile strength of 3.9 MPa at 3% content, which was 21.8% higher than that of PCL scaffold, and compressive strength of 3.7 MPa at 25% strain, a 32.1% improvement over the PCL scaffold. Besides, the water

absorption of the composite scaffold was improved, which promoted the degradation to a certain extent. Mineralization experiments showed that the composite scaffold exhibited the ability to grow with apatite in simulated body fluids, which facilitated the formation of a biological bond with the natural bone after implantation. Our preliminary results indicate that the PCL/TM scaffold can be used in bone tissue engineering and could be investigated as a novel composite material.

## Conflicts of interest

The authors declare that they have no known competing financial interests or personal relationships that could have appeared to influence the work reported in this paper.

## Acknowledgements

This work was supported by the following funds: (1) Natural Science Foundation of Hunan Provincial (2021JJ30632, 2022JJ50182, 2020JJ4556); (2) Scientific Research Foundation of Hunan Provincial Education Department (21B0686); (3) Research Foundation of Shaoyang Science and Technology Bureau (2021GZ041); (4) Program of National Student Innovation and Entrepreneurship (202210547004); (5) Graduate Research and Innovation Project of Hunan Provincial (CX20221316); (6) Graduate Research and Innovation Project of Shaoyang University (CX2022SY003).

## References

- 1 D. Li, M. Chen, W. Guo, *et al.*, In Situ Grown Nanohydroxyapatite Hybridized Graphene Oxide: Enhancing the Strength and Bioactivity of Polymer Scaffolds, *ACS Omega*, 2022, 7(14), 12242–12254.
- 2 D. Li, P. Li, Y. Xu, *et al.*, Progress in Montmorillonite Functionalized Artificial Bone Scaffolds: Intercalation and Interlocking, Nanoenhancement, and Controlled Drug Release, *J. Nanomater.*, 2022, 2022, 7900382.
- 3 P. Feng, M. Liu, S. Peng, *et al.*, Polydopamine modified polycaprolactone powder for fabrication bone scaffold owing intrinsic bioactivity, *J. Mater. Res. Technol.*, 2021, 15, 3375–3385.
- 4 P. Zhang, Y. Xin, F. Ai, *et al.*, Preparation and properties of multi-walled carbon nanotubes and eggshell dual-modified polycaprolactone composite scaffold, *J. Polym. Eng.*, 2019, 39(4), 343–350.
- 5 R. D. Juliana, S. Aureliana, A. Ana, *et al.*, Electrospun Polycaprolactone (PCL) Degradation: An In Vitro and In Vivo Study, *Polymers*, 2022, 14(16), 3397.
- 6 M. S. G. Stacey, M. Sumit, G. Paulomi, *et al.*, Direct 3D printing of decellularized matrix embedded composite polycaprolactone scaffolds for cartilage regeneration, *Biomater. Adv.*, 2022, 140, 213052.
- 7 L. Wang, C. Wang, L. Zhou, *et al.*, Fabrication of a novel three-dimensional porous PCL/PLA tissue engineering scaffold with high connectivity for endothelial cell migration, *Eur. Polym. J.*, 2021, 161, 110834.



- 8 A. K. Matta, R. U. Rao, K. N. S. Suman, *et al.*, Preparation and Characterization of Biodegradable PLA/PCL Polymeric Blends, *Procedia Mater. Sci.*, 2014, **6**, 1266–1270.
- 9 S. Wachirahuttapong, C. Thongpin and N. Sombatsompop, Effect of PCL and Compatibility Contents on the Morphology, Crystallization and Mechanical Properties of PLA/PCL Blends, *Energy Procedia*, 2016, **89**, 198–206.
- 10 Y. H. A. Wu, Y. C. Chiu, Y. H. Lin, *et al.*, 3D-Printed Bioactive Calcium Silicate/Poly-Epsilon-Caprolactone Bioscaffolds Modified with Biomimetic Extracellular Matrices for Bone Regeneration, *Int. J. Mol. Sci.*, 2019, **20**(4), 942.
- 11 Z. Du, H. Leng, L. Guo, *et al.*, Calcium silicate scaffolds promoting bone regeneration via the doping of  $Mg^{2+}$  or  $Mn^{2+}$  ion, *Composites, Part B*, 2020, **190**, 107937.
- 12 Y. Chen, S. Wang, Y. Li, *et al.*, Adsorption of Pb(II) by tourmaline-montmorillonite composite in aqueous phase, *J. Colloid Interface Sci.*, 2020, **575**, 367–376.
- 13 L. X. Fu, Y. Guo, Q. H. Zhang, *et al.*, Tourmaline@ZnO Core-Shell Structural Composites: Fabrication, Characterization, and Optical Properties, *J. Electron. Mater.*, 2018, **47**(8), 4289–4295.
- 14 J. Liang, N. Hui, T. Zhao, *et al.*, The mineralization of polymer electrospun fibrous membranes modified with tourmaline nanoparticles, *J. Mater. Res.*, 2019, **34**(11), 1900–1910.
- 15 B. Yu, J. Han, H. Sun, *et al.*, The preparation and property of poly(lactic acid)/tourmaline blends and melt-blown nonwoven, *Polym. Compos.*, 2015, **36**(2), 264–271.
- 16 L. D. Tijing, M. T. G. Ruelo, A. Amarjargal, *et al.*, Antibacterial and superhydrophilic electrospun polyurethane nanocomposite fibers containing tourmaline nanoparticles, *Chem. Eng. J.*, 2012, **197**, 41–48.
- 17 P. Georgopoulos, E. Eichner, V. Filiz, *et al.*, Improvement of mechanical properties by a polydopamine interface in highly filled hierarchical composites of titanium dioxide particles and poly(vinyl butyral), *Compos. Sci. Technol.*, 2017, **146**, 73–82.
- 18 Y. Hu and X. Yang, The surface organic modification of tourmaline powder by span-60 and its composite, *Appl. Surf. Sci.*, 2012, **258**(19), 7540–7545.
- 19 Y. Hu, The Studies on the Surface Organic Modification of Tourmaline Powder with Stearic Acid and Its Composite, *Open J. Compos. Mater.*, 2014, **04**(03), 148–156.
- 20 H.-I. Hsiang, L.-F. Fan and J.-J. Hung, Effects of the sodium stearate addition on the corrosion resistance and electromagnetic properties of phosphatized iron-based SMCs, *J. Magn. Magn. Mater.*, 2019, **490**, 165532.
- 21 Q. Tang, Y.-M. Zhang, P.-G. Zhang, *et al.*, Preparation and properties of thermal insulation coatings with a sodium stearate-modified shell powder as a filler, *Int. J. Miner. Metall. Mater.*, 2017, **24**(10), 1192–1199.
- 22 T.-C. Lin, K.-C. Yang, P. Georgopoulos, *et al.*, Gyroid-structured nanoporous polymer monolith from PDMS-containing block copolymers for templated synthesis, *Polymer*, 2017, **126**, 360–367.
- 23 S. Catchpole-Smith, R. R. J. Sélo, A. W. Davis, *et al.*, Thermal conductivity of TPMS lattice structures manufactured via laser powder bed fusion, *Addit. Manuf.*, 2019, **30**, 100846.
- 24 Z. Cai, Z. Liu, X. Hu, *et al.*, The effect of porosity on the mechanical properties of 3D-printed triply periodic minimal surface (TPMS) bioscaffold, *Bio-Des. Manuf.*, 2019, **2**(4), 242–255.
- 25 F. Perez-Boerema, M. Barzegari and L. Geris, A flexible and easy-to-use open-source tool for designing functionally graded 3D porous structures, *Virtual and Physical Prototyping*, 2022, **17**(3), 682–699.
- 26 J. Iamsamang and P. Naiyanetr, Computational method and program for generating a porous scaffold based on implicit surfaces, *Computer Methods and Programs in Biomedicine*, 2021, **205**, 106088.
- 27 R. Verma, J. Kumar, N. K. Singh, *et al.*, Design and Analysis of Biomedical Scaffolds Using TPMS-Based Porous Structures Inspired from Additive Manufacturing, *Coatings*, 2022, **12**(6), 839.
- 28 A. Panesar, M. Abdi, D. Hickman, *et al.*, Strategies for functionally graded lattice structures derived using topology optimisation for additive manufacturing, *Addit. Manuf.*, 2018, **19**, 81–94.
- 29 G. Li, D. Chen, W. Zhao, *et al.*, Efficient adsorption behavior of phosphate on La-modified tourmaline, *J. Environ. Chem. Eng.*, 2015, **3**(1), 515–522.
- 30 F. Wang, Z. Xie, J. Liang, *et al.*, Tourmaline-Modified FeMnTiO<sub>x</sub> Catalysts for Improved Low-Temperature NH<sub>3</sub>-SCR Performance, *Environ. Sci. Technol.*, 2019, **53**(12), 6989–6996.
- 31 Y. Deng, M. Zhang, X. Chen, *et al.*, A novel akermanite/poly(lactic-co-glycolic acid) porous composite scaffold fabricated via a solvent casting-particulate leaching method improved by solvent self-proliferating process, *Regener. Biomater.*, 2017, **4**(4), 233–242.
- 32 S. H. Lee, K. G. Lee, J. H. Hwang, *et al.*, Evaluation of mechanical strength and bone regeneration ability of 3D printed kagome-structure scaffold using rabbit calvarial defect model, *Mater. Sci. Eng., C*, 2019, **98**, 949–959.
- 33 A. Diaz-Arca, P. Ros-Tarraga, M. J. M. Tome, *et al.*, Micro-/Nano-Structured Ceramic Scaffolds That Mimic Natural Cancellous Bone, *Materials*, 2021, **14**(6), 1439.
- 34 W. Liao, Z. Shan and J. Tian, Facile Fabrication of Fe<sub>3</sub>O<sub>4</sub>@TiO<sub>2</sub>@C Yolk-Shell Spheres as Anode Material for Lithium Ion Batteries, *Trans. Tianjin Univ.*, 2019, **26**(1), 3–12.
- 35 Y. U. Liang, S. Sun, H. Ding, *et al.*, Preparation and Characterization of Organic Modified Calcium Carbonate by Sodium Stearate (Or Sodium Oleate) Using Wet Method, *Surf. Rev. Lett.*, 2020, **27**(10), 1950224.
- 36 L. Du, Y. Wang and G. Luo, In situ preparation of hydrophobic CaCO<sub>3</sub> nanoparticles in a gas-liquid microdispersion process, *Particuology*, 2013, **11**(4), 421–427.
- 37 H. Fan, X. Song, Y. Xu, *et al.*, Insights into the modification for improving the surface property of calcium sulfate whisker: experimental and DFT simulation study, *Appl. Surf. Sci.*, 2019, **478**, 594–600.



- 38 A. Fakhrali, M. Nasari, N. Poursharifi, *et al.*, Biocompatible graphene-embedded PCL/PGS-based nanofibrous scaffolds: a potential application for cardiac tissue regeneration, *J. Appl. Polym. Sci.*, 2021, **138**(40), 51177.
- 39 R. Soni, N. V. Kumar, S. Chameettachal, *et al.*, Synthesis and Optimization of PCL-Bioactive Glass Composite Scaffold for Bone Tissue Engineering, *Mater. Today: Proc.*, 2019, **15**, 294–299.
- 40 Z. Xie, F. Wang, J. Liang, *et al.*, Enhanced catalytic efficiency of FeMnTiO<sub>x</sub> SCR catalysts through adding tourmaline nanopowders during the one-step sol-gel process, *Mater. Lett.*, 2018, **217**, 60–63.

